Nearshore sandbar migration predicted by an eddy-diffusive boundary layer model

Stephen M. Henderson,[1] J. S. Allen, and P. A. Newberger
College of Oceanic and Atmospheric Sciences, Oregon State University, Corvallis, Oregon, USA

Received 22 September 2003; revised 5 March 2004; accepted 1 April 2004; published 23 June 2004.

[1] We simulated the erosion and accretion of a natural beach using a wave-resolving eddy-diffusive model of water and suspended sediment motion in the bottom boundary layer. Nonlinear advection was included in this one-dimensional (vertical profile) model by assuming that waves propagated almost without change of form. Flows were forced by fluctuating pressure gradients chosen to reproduce the velocity time series measured during the Duck94 field experiment. The cross-shore flux of suspended sediment beneath each field-deployed current meter was estimated, and beach erosion (accretion) was calculated from the divergence (convergence) of this flux. Horizontal pressure forces on sediment particles were neglected. The model successfully predicted two bar migration events (one shoreward bar migration and one seaward) but failed to predict a third (seaward migration) event. Simulated seaward sediment transport was due to seaward mean currents. Simulated shoreward sediment transport was due to covariance between wave-frequency fluctuations in velocity and sediment concentration and was mostly confined to the wave boundary layer. Predicted seaward (shoreward) bar migration was driven by a maximum in the current-generated (wave-generated) flux over the sandbar. A wave-generated downward flux of shoreward momentum into the wave boundary layer contributed to shoreward sediment transport and often had a local maximum over the bar crest. Second-order nonlinear advection of sediment, mostly representing shoreward advection by the Stokes drift, also often had a local maximum over the bar crest. Together, wave-generated momentum fluxes and the Stokes drift substantially increased shoreward transport and were essential to predictions of shoreward bar migration. *INDEX TERMS:* 4546 Oceanography: Physical: Nearshore processes; 4255 Oceanography: General: Numerical modeling; 4558 Oceanography: Physical: Sediment transport; 3022 Marine Geology and Geophysics: Marine sediments—processes and transport; 3020 Marine Geology and Geophysics: Littoral processes; *KEYWORDS:* sediment transport, benthic boundary layers, beach erosion

Citation: Henderson, S. M., J. S. Allen, and P. A. Newberger (2004), Nearshore sandbar migration predicted by an eddy-diffusive boundary layer model, *J. Geophys. Res.*, *109*, C06024, doi:10.1029/2003JC002137.

1. Introduction

[2] Predictions of beach erosion and accretion are important to coastal planners and engineers. This paper introduces a model that simulates beach erosion and accretion using time series of water velocity measured near (about 0.5 m above) the seabed.

[3] Standard sediment transport models that are based on the "energetics" approach of *Bagnold* [1966] sometimes fail to simulate field-observed beach erosion and accretion. Under the assumption that the energy expended by steady flows in transporting sediment is proportional to the total dissipation, *Bagnold* [1966] derived a formula relating the sediment transport rate to the water velocity. *Bowen* [1981] and *Bailard* [1981] suggested that the average sediment flux under waves can be predicted by substituting instantaneous water velocities into a simplified version of Bagnold's formula, and time-averaging the resulting instantaneous flux estimates. *Thornton et al.* [1996] substituted water velocities measured during the DELILAH field experiment of 1990 into Bailard's sediment transport formula to predict the erosion and accretion of a natural beach near Duck, North Carolina. On this beach, Bailard's model successfully predicted the formation and seaward migration of a shore-parallel sandbar that was observed during two storms. However, Bailard's model did not predict the minor beach erosion and accretion events that were observed between storms. *Gallagher et al.* [1998] tested Bailard's model using data collected during the Duck94 field experiment of 1994. Again, Bailard's model successfully predicted the erosion and seaward bar migration observed during storms. However, Bailard's model failed to predict a substantial shoreward bar migration event which was observed when

[1]Now at Scripps Institution of Oceanography, Center for Coastal Studies, University of California, San Diego, La Jolla, California, USA.

0148-0227/04/2003JC002137$09.00

waves were moderately energetic and mean currents were weak. According to Bailard's model, the seaward bar migration observed during these experiments was driven primarily by a maximum in the seaward directed mean current (the "undertow") near the bar crest. Predicted wave-generated transport was relatively weak, but tended to reinforce bar generation and seaward migration during storms.

[4] Several researchers have suggested mechanisms that might cause shoreward bar migration. *Trowbridge and Young* [1989] suggested that nonlinear wave boundary layer processes might play a role. The wave boundary layer is a region, usually extending 5–10 cm above the seabed, where friction leads to strongly rotational wave-frequency flows. Shoreward propagating waves carry a vertical flux of shoreward momentum into the wave boundary layer, thereby forcing a shoreward mean Eulerian "streaming" flow near the bed (see *Longuet-Higgins* [1953] and Longuet-Higgins' appendix to *Russell and Osorio* [1957]). *Trowbridge and Young* [1989] showed that, under moderately energetic waves, the wave-generated flux of momentum into the wave boundary layer has a local maximum over the sandbar. They suggested that this would lead to a maximum in shoreward sediment transport over the bar, and shoreward bar migration. *Trowbridge and Young*'s [1989] model successfully predicted a shoreward bar migration event that was observed on a natural beach, but excludes sediment transport by the undertow, and fails to predict seaward bar migration. Under nonsinusoidal waves, a covariance between eddy viscosity and velocity shear might complicate the boundary layer streaming described above. *Trowbridge and Madsen* [1984] showed that such a covariance would generate a mean stress which might modify, and even reverse, the Eulerian streaming.

[5] In addition to driving shoreward boundary layer streaming, waves also transport sediment through a second-order "Stokes drift" (*Phillips* [1977, section 3.3] discusses the Stokes drift; *van Hardenberg et al.* [1991] and *Deigaard et al.* [1999] discuss the resulting sediment advection). Like Eulerian boundary layer streaming, the Stokes drift is directed shoreward and, under moderately energetic waves, has a local maximum over the crest of the sandbar. Therefore, we suggest that the Stokes drift might play a role in driving shoreward bar migration. The Stokes drift is of the same order as Eulerian boundary layer streaming. Furthermore, cross-shore mass balance ensures that the Stokes drift is of the same order as the undertow. Therefore, to be formally consistent, models of suspended sediment transport must include (or exclude) undertow, Stokes drift, and boundary layer streaming simultaneously.

[6] Shoreward bar migration might also be caused by the systematic changes in waveshape that occur over the bar. Waveshapes are often described as "skewed" or "asymmetric" [*Elgar*, 1987]. Waves with positive skewness have sharp, high peaks and broad, shallow troughs. Waves with positive asymmetry are pitched forward, with steep leading faces and gently sloped rear faces. As waves pitch forward and break, time series of sea level and shoreward water velocity become strongly asymmetric. Water velocity asymmetry is related closely to acceleration skewness, and time series of acceleration are strongly skewed under breaking waves. *Elgar et al.* [2001] noted that acceleration skewness tends to be maximum over the sandbar (where breaking tends to be intense), and suggested that transport proportional to acceleration skewness might be responsible for shoreward bar migration. *Hoefel and Elgar* [2003] showed that addition of acceleration-skewness-dependent transport to the model of *Bailard* [1981] leads to successful predictions of both the shoreward and the seaward bar migration observed during the Duck94 experiment.

[7] The mechanism by which transport might depend on acceleration skewness remains unclear. Outside the wave boundary layer, the acceleration is roughly proportional to the pressure gradient. Consequently, acceleration skewness might be associated with net sediment transport through the action of pressure gradients on sediment particles [*Drake and Calantoni*, 2001; *Madsen*, 1975; *Sleath*, 1999]. According to this hypothesis, the strong horizontal pressure gradients under the steep front faces of broken waves force sediment shoreward. In contrast, the weak pressure gradients under the gently sloped rear faces of broken waves are said to be relatively ineffective at forcing sediment seaward. An alternative hypothesis was proposed by *Nielsen* [1992, pp. 121–128], who suggested that transport under waves with skewed accelerations can be predicted from the bed shear stress, without reference to the horizontal pressure gradient. According to the hypothesis of *Nielsen* [1992], transport under asymmetric waves is due to a negative correlation between the shoreward water velocity and the boundary layer thickness; a thinner boundary layer is associated with a higher shear stress, and increased sediment transport. *Nielsen and Callaghan* [2003] suggested that the model of *Nielsen* [1992] might represent both pressure gradient and boundary layer thickness effects. A third hypothesis, possibly related to *Nielsen*'s [1992] hypothesis, was proposed by *Puleo et al.* [2003]. They suggested that a correlation between turbulence intensity (and therefore the suspended sediment concentration) and acceleration might be responsible for acceleration-dependent transport in the swash zone.

[8] In this paper, we test the ability of a model that simulates boundary layer dynamics, but neglects the effects of horizontal pressure forces on sediment particles, to predict field-observed sandbar migration. The model uses a two-equation turbulence closure to solve the boundary layer equations for water and suspended sediment motion. Second-order wave-generated momentum fluxes are included in the momentum equation, so boundary layer streaming is simulated. Furthermore, second-order wave-generated advection is included in the sediment conservation equation, so transport by the Stokes drift is simulated. Momentum fluxes and second-order sediment advection have been neglected by most previous boundary layer models that are based on two-equation turbulence closures [e.g., *Davies et al.*, 2002; *Holmedal et al.*, 2003]. However these processes were simulated, for the idealised case of slowly varying sinusoidal waves, by the mixing length model of *Deigaard et al.* [1999]. Our model is derived in section 2, and the field site and instrumentation are described in section 3.

Predictions of sediment transport and beach evolution are presented in section 4. The model successfully predicted two bar migration events (including a shoreward bar migration event), but failed to predict a third. The mechanisms responsible for the predicted sediment transport are discussed in section 5. A phase shift between near-bed and free-stream velocity led to asymmetry-dependent near-bed sediment transport. Both momentum fluxes and the Stokes drift were important to predictions of shoreward bar migration. Conclusions are presented in section 6.

2. Model Derivation

2.1. Hydrodynamic Model

[9] In this section, we derive a set of one-dimensional equations for conservation of water mass and momentum in nearshore bottom boundary layers. The primitive boundary layer equations are

$$\frac{\partial u_j^*}{\partial t^*}+\frac{\partial u_k^* u_j^*}{\partial x_k^*}+\frac{\partial w^* u_j^*}{\partial z^*}+\frac{1}{\rho_w^*}\frac{\partial p^*}{\partial x_j^*}=\frac{\partial}{\partial z^*}\left(\nu^*\frac{\partial u_j^*}{\partial z^*}\right), \quad (1)$$

$$\frac{\partial u_k^*}{\partial x_k^*}+\frac{\partial w^*}{\partial z^*}=0, \quad (2)$$

where stars indicate dimensional variables, x_1^*, x_2^* and z^* are cross-shore, longshore and boundary-normal coordinates (x_1^* positive onshore), u_j^* and w^* are respectively the x_j^* and z^* components of the water velocity, ρ_w^* is the water density, and p^* is the pressure (independent of z^*). Turbulent mixing of momentum has been parameterised using an eddy viscosity ν^*. The summation convention has been used, so repeated indices are summed over allowable values (1 and 2).

[10] Let the dimensional constants k_0, ν_0, u_0, and c_0 respectively represent the typical wave number, eddy viscosity, water speed, and wave phase speed. The approximate wave boundary layer thickness is $\delta_0=[\nu_0/(k_0c_0)]^{1/2}$. In terms of the dimensionless variables

$$t=k_0c_0t^*,$$
$$x_j=k_0x_j^*,$$
$$z=\frac{z^*}{\delta_0},$$
$$u_j=\frac{u_j^*}{u_0},$$
$$w=\left(\frac{1}{k_0\delta_0}\right)\frac{w^*}{u_0},$$
$$p=\frac{p^*}{\rho_w^*u_0c_0},$$
$$\nu=\frac{\nu^*}{\nu_0},$$
$$\sigma^2=\frac{u_0}{c_0},$$

equations (1) and (2) are

$$\frac{\partial u_j}{\partial t}+\sigma^2\left(\frac{\partial u_ku_j}{\partial x_k}+\frac{\partial wu_j}{\partial z}\right)+\frac{\partial p}{\partial x_j}=\frac{\partial}{\partial z}\left(\nu\frac{\partial u_j}{\partial z}\right), \quad (3)$$

$$\frac{\partial u_k}{\partial x_k}+\frac{\partial w}{\partial z}=0. \quad (4)$$

The constant σ^2 determines the importance of the momentum flux.

[11] Equations (3) and (4) are three-dimensional, and their numerical solution requires a great deal of computational time. Next, we will develop a more computationally efficient model by reducing equations (3) and (4) to a system of one-dimensional equations for the vertical profile of the water velocity.

[12] We assume that $\sigma^2 \ll 1$, so momentum fluxes are weak. However, we do not wish to neglect momentum fluxes entirely, because they might play an important role in driving shoreward bar migration [*Trowbridge and Young*, 1989]. Instead, we will expand equations (3) and (4), retaining terms to order σ^2. We divide the flow into wave and low frequency components, denoted respectively by a tilde ($\tilde{\cdot}$) and an overbar ($\bar{\cdot}$). Formally, we say that the low frequency flow is a function of only the slow time $t_s=\sigma^2t$. In addition to assuming that momentum fluxes are weak, we require:

[13] 1. Water depths, wave amplitudes and low-frequency flows vary over spatial scales much longer than a wavelength. Formally, they are functions of the slow variable $x_s=\sigma^2x$.

[14] 2. The water is so shallow that the Boussinesq approximations hold (k_0h^* is order σ, where h^* is the mean water depth). Consequently, the dimensionless phase speed $c=c^*/c_0=1+O(\sigma^2)$, where c^* is the dimensional phase speed, $c_0=(g^*h^*)^{1/2}$, and g^* is the gravitational acceleration [e.g., *Mei*, 1989, pp. 510–511].

[15] 3. Waves propagate almost directly shoreward, so wave angles are order σ (if waves propagate from deep water onto a longshore-uniform beach, then this follows from the Boussinesq approximation [*Herbers and Burton*, 1997]). It follows that longshore wave velocities are small (order σ), but longshore mean currents may be strong. Longshore derivatives of both components of wave velocity are small.

[16] Assumptions 1–3 above, and the assumption $\sigma^2 \ll 1$, are often used in models that predict wave evolution across the surf zone [e.g., *Herbers and Burton*, 1997].

[17] Our aim is to remove the horizontal derivatives from equations (3) and (4). First we consider the term $\partial(u_1u_2)/\partial x_1$. From assumption 3

$$\frac{\partial u_1u_2}{\partial x_1}=\frac{\partial u_1\bar{u}_2}{\partial x_1}+O(\sigma). \quad (5)$$

From equation (5) and assumption 1

$$\frac{\partial u_1u_2}{\partial x_1}=\frac{\partial\tilde{u}_1}{\partial x_1}\bar{u}_2+O(\sigma). \quad (6)$$

From assumptions 1–3, waves change their form only slowly as they propagate shoreward, so

$$\frac{\partial \tilde{u}_1}{\partial x_1} = -\frac{\partial \tilde{u}_1}{\partial t} + O(\sigma^2), \tag{7}$$

or, in dimensional form,

$$\frac{\partial \tilde{u}_1^*}{\partial x_1^*} = -\frac{1}{c_0}\frac{\partial \tilde{u}_1^*}{\partial t^*} + O(\sigma^2). \tag{8}$$

This relation has been used in many theories for waves of permanent form [*Mei*, 1989, section 11.5], and also was used in the wave boundary layer models of *Trowbridge and Madsen* [1984] and *Deigaard et al.* [1999]. Recalling that time derivatives of low frequency flows are small, and that the longshore wave velocity is weak, substituting equation (7) into equation (6) leads to

$$\frac{\partial u_1 u_2}{\partial x_1} = -\frac{\partial u_1 u_2}{\partial t} + O(\sigma). \tag{9}$$

A similar identity holds for the term $\partial u_1^2/\partial x_1$. From assumptions 1 and 3, longshore derivatives are small, so the terms $\sigma^2\partial(u_2u_j)/\partial x_2$ are at most order σ^3. Discarding terms of order σ^3 leads to the one-dimensional momentum equations

$$\frac{\partial u_j}{\partial t} + \sigma^2\left(-\frac{\partial u_1 u_j}{\partial t} + \frac{\partial w u_j}{\partial z}\right) + \frac{\partial p}{\partial x_j} = \frac{\partial}{\partial z}\left(\nu\frac{\partial u_j}{\partial z}\right). \tag{10}$$

A similar derivation leads to the one-dimensional mass conservation equation

$$\frac{\partial u_1}{\partial t} - \frac{\partial w}{\partial z} = O(\sigma^2). \tag{11}$$

Integrating equation (11) vertically gives a leading-order estimate for w, which is substituted into equation (10) to calculate $\partial u_j/\partial t$ with error $O(\sigma^3)$.

[18] The eddy viscosity ν was calculated using a k-ϵ turbulence closure (Appendix A). Turbulent energy levels and turbulent dissipation rates were updated every time step (every hundredth of a second). Consequently, *Trowbridge and Madsen*'s [1984] streaming mechanism was resolved. We assumed zero diffusive flux of turbulent energy across the upper boundary of the model, thereby excluding any addition of turbulent energy to the near-bed region by wave breaking. On the basis of field-observed longshore momentum balances, *Feddersen et al.* [2003] suggested that wave breaking substantially increases near-bed turbulence and bed stress. In contrast, *Trowbridge and Elgar* [2001] found that field-observed turbulent dissipation within a meter of the bed beneath breaking waves approximately balanced local production (this balance would not hold if much turbulent energy was injected from above).

[19] The bottom boundary condition for u_j was derived by assuming a logarithmic velocity profile below the computational domain, with the velocity tending to zero at a roughness height z_0. This leads to the stress condition described in the work of *Mellor* [2002, Appendix A]. The roughness height is influenced by bedforms and by saltating sand grains, but no method for predicting the roughness height has achieved universal acceptance (instead, several conflicting models [*Sleath*, 1984; *Nielsen*, 1992; *Soulsby*, 1997] have been proposed). Most results presented in this paper simply assume that $z_0 = 10^{-3}$ m. This corresponds to a Nikuradse roughness length of 3 cm, which is comparable to the height of nearshore bedforms [*Gallagher et al.*, 2003]. We will test the sensitivity to z_0 using results obtained with $z_0 = 3 \times 10^{-4}$ m and $z_0 = 3 \times 10^{-3}$ m. We will neglect spatial and temporal variations in z_0.

[20] We will simulate the boundary layer flows that occur under field-observed waves. To do this, we chose a computational domain that extends from an elevation $z_l = 2z_0$ very near the seabed to the elevation z_c of a current meter. The time series of water velocity measured by the current meter provides the upper boundary condition for our model. It remains to calculate a horizontal pressure gradient which is consistent with the observed water velocity time series. To do this, we assume that the current meter is outside the wave boundary layer, so $\partial\tilde{u}/\partial z \approx 0$. We also assume that the current meter is inside the constant stress layer of the low frequency flow, so

$$\frac{\partial}{\partial z}\left(\nu\frac{\partial u_j}{\partial z}\right)\bigg|_{z=z_c} \approx \frac{\partial}{\partial z}\left(\nu\frac{\partial \overline{u}_j}{\partial z}\right)\bigg|_{z=z_c} = 0. \tag{12}$$

This final approximation is inaccurate for low frequency flows associated with infragravity and shear waves.

[21] The derivation of a formally consistent boundary layer model has led to exclusion of both the mean pressure gradient associated with setup, and the mean momentum flux gradient associated with spatial variations in the wave field [e.g., *Deigaard and Fredsøe*, 1989]. This provides a good approximation near the seabed (i.e., where the elevation above the bed is a sufficiently small fraction of the depth), but a poor approximation farther above the bed. The upper boundary of our model domain is the elevation z_c of a current meter. Usually, current meters were deployed fairly near the bed (z_c was about a quarter of the water depth), so the boundary layer approximation may have been accurate. However, occasionally current meters were deployed farther from the bed (z_c up to about half the water depth), so the boundary layer approximation was inaccurate. In these cases, we expect that the neglected mean pressure gradient (which, inside the surf zone, forces water seaward) exceeded the neglected mean momentum flux gradient (which, inside the surf zone, forces water shoreward), so that seaward flows and seaward sediment transport were underpredicted. A formally consistent relaxation of the boundary layer approximation would require solution of the undertow problem, and is beyond the scope of this paper.

[22] We calculated second-order accurate pressure gradients from equation (12) and the measured velocities using an iterative approach (Appendix B). Equations (10) and (11), together with the turbulence closure, were then solved using a finite difference scheme.

2.2. Sediment Transport Model

[23] Under the assumptions introduced in section 2.1, an equation for conservation of suspended sediment is [cf.

Fredsoe and Deigaard, 1992, equation 8.45; *Deigaard et al.*, 1999, equations 27 and 28]

$$\frac{\partial \mathcal{C}}{\partial t^*} - \frac{1}{c_0}\frac{\partial u_1^* \mathcal{C}}{\partial t^*} + \frac{\partial (w^* - w_s^*)\mathcal{C}}{\partial z^*} = \frac{\partial}{\partial z^*}\left(\nu^* \frac{\partial \mathcal{C}}{\partial z^*}\right), \tag{13}$$

where $\mathcal{C}$ is the sediment concentration and w_s^* is the sediment fall velocity (a constant, here calculated from the grain diameter using the formula of *Gibbs et al.* [1971]). Turbulent mixing of sediment has been parameterised using an eddy diffusivity equal to the eddy viscosity ν^*.

[24] At the upper boundary ($z = z_c$), we assume

$$w_s^* \mathcal{C} + \nu^* \frac{\partial \mathcal{C}}{\partial z^*} = 0, \tag{14}$$

so sediment settling balances upward mixing.

[25] At the lower boundary ($z = z_l$), we specify the upward turbulent mixing of sediment

$$-\nu^* \frac{\partial \mathcal{C}}{\partial z^*} = \begin{cases} \zeta w_s^* \mathcal{C}_{\text{ref}} & \tau > \tau_c \\ 0 & \tau \le \tau_c \end{cases}, \tag{15}$$

where

$$\zeta = \left(\frac{z_l}{2D}\right)^{-\gamma}, \tag{16}$$

$$\gamma = \frac{w_s^*}{\kappa(\tau/\rho_w^*)^{1/2}}, \tag{17}$$

$$\mathcal{C}_{\text{ref}} = \alpha\left(\frac{\tau - \tau_c}{\tau_c}\right)^{\beta}, \tag{18}$$

τ is the magnitude of the bed shear stress, τ_c is the critical shear stress (calculated by assuming a critical Shields parameter of 0.05), D is the sediment grain diameter, and $\kappa = 0.4$ is von Karman's constant. The constant α is chosen to calibrate the model, as described in section 3. $\mathcal{C}_{\text{ref}}$ is the reference concentration which would be achieved under steady flow at an elevation two grain diameters above the bed. ζ represents the vertical attenuation of sediment concentration from an elevation two grain diameters above the bed (where $\mathcal{C}_{\text{ref}}$ is specified) to the base of the numerical grid z_l (where equation (15) is applied). This attenuation was derived by assuming a Rouse concentration profile beneath the numerical grid [*Rouse*, 1937].

[26] Consider a steady flow, with $\nu^* = \kappa z^*(\tau/\rho_w^*)^{1/2}$. Let ρ_s^* equal the density of a sand grain. Now, given concentrations much less than one, the pickup function (15) with $\beta = 1$ and $\alpha = (1.6 \times 10^{-3})$ $(\rho_s^* - \rho_w^*)/\rho_w^*$ resembles the reference concentration condition of *Smith and McLean* [1977] (differences arise because we applied equation (15) at $z = 2D$, whereas *Smith and McLean* [1977] apply their condition at an elevation that depends on the shear stress, and because we neglected any difference between the total stress and the effective stress). Alternatively, setting $\beta = 1.5$ and choosing an appropriate (constant) value for α gives the pickup function of *van Rijn* [1984]. Most results presented in the remainder of this paper assume $\beta = 1$. However, we will test the sensitivity to β by comparing the skill of bar migration predictions obtained when $\beta = 1$ with the skill obtained when $\beta = 1.5$.

[27] The mean sediment flux in direction x_j occurring within a distance z_t of the seabed is roughly

$$q_j^* = \int_{z^*=z_l}^{z_t} \langle u_j^* \mathcal{C} \rangle \, dz^*, \tag{19}$$

where angle brackets denote a time average. The flux beneath z_l has been neglected. Therefore bedload transport has been excluded from the predicted sediment flux. The importance of bedload transport to beach profile evolution is unknown. Energetics-based models predict that bedload transport is small [*Gallagher et al.*, 1998]. *Conley and Beach* [2003] found that field-observed suspended sediment transport was of the same order as total transport (estimated from bathymetric changes). In contrast, *Janssen et al.* [1998] found that bedload dominated the total transport measured in a large oscillating water tunnel. The suspended flux between z_0 and z_l has also been neglected, but is very small. The choice of z_t represents a compromise between two competing requirements. First, z_t must be large enough to ensure that the sediment flux above z_t, which is excluded from equation (19), is negligible. Second, z_t must lie within the model domain, which extends from very near the bed to the elevation of a current meter. When the elevation of a current meter was less than z_t, data from that current meter had to be discarded. We chose $z_t = 0.35$ m. Usually the Eulerian flux $\langle u_j^* \mathcal{C} \rangle$ was very small at z_t, indicating that the flux above z_t was negligible. However, occasionally (during periods of rapid seaward transport) $\langle u_j^* \mathcal{C} \rangle$ was not very small at z_t, and the total depth-integrated flux was probably greater than q_j^*.

3. Field Observations

[28] We will compare the beach erosion and accretion predicted by the model derived in section 2 with the erosion and accretion observed during the Duck94 field experiment of 1994 [*Elgar et al.*, 1997; *Gallagher et al.*, 1998]. During this experiment, 2-Hz time series of horizontal water velocity were measured at 14 locations along a cross-shore transect extending from the shore to about 5-m depth (Figure 1). Small current meter orientation errors were corrected as described by *Herbers et al.* [1999]. A further 3.7-degree correction removed the difference between the Field Research Facility's coordinate system and the longshore and cross-shore coordinates estimated using surveys from an amphibious vehicle [*Lee and Birkemeier*, 1993]. The seabed elevations used to test model predictions were measured using sonar altimeters [*Gallagher et al.*, 1996] that were colocated with the current meters.

[29] For most simulations presented in this paper, the cross-shore variation of sand grain diameter was assumed independent of time, and was estimated by fitting a smooth curve through the field measurements described by *Stauble and Cialone* [1997] (Figure 2). The assumption that the grain diameter depends on cross-shore location is not strictly consistent with the assumption that the grain diam-

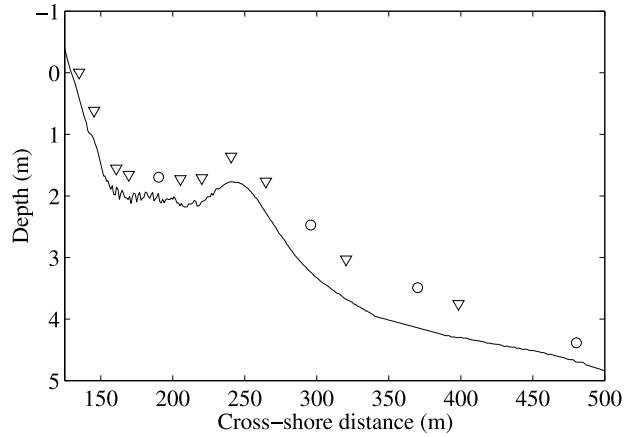

Figure 1. Beach profile measured by an amphibious vehicle [*Lee and Birkemeier*, 1993] on 21 September (solid curve), and cross-shore locations of instruments. Circles indicate current meters; triangles indicate colocated current meters and sonar altimeters.

eter does not depend on time. Nevertheless, these two assumptions have been adopted simultaneously by previous researchers [*Gallagher et al.*, 1998; *Hoefel and Elgar*, 2003]. We will test the sensitivity to cross-shore variations in grain diameter by rerunning the model with a constant grain diameter of 2×10^{-4} m.

[30] The model derived in section 2 was run repeatedly, once for every instrument location and for every three-hour time series between 1 September and 11 October (10^{-2} s leapfrog time step, total CPU time about 12 days on a 500 MHz Compaq Alpha XP1000). The stress exponent β in equation (18), and the bottom roughness z_0, were respectively set to 1 and 1×10^{-3} m unless otherwise stated. Every three hours, the mean sediment flux q_j^* was calculated at each instrument location using equation (19). A continuous cross-shore profile of shoreward sediment flux $\hat{q}_1^*$ was estimated for cross-shore locations between 150 m and 450 m (Figure 1) by fitting a weakly smoothing

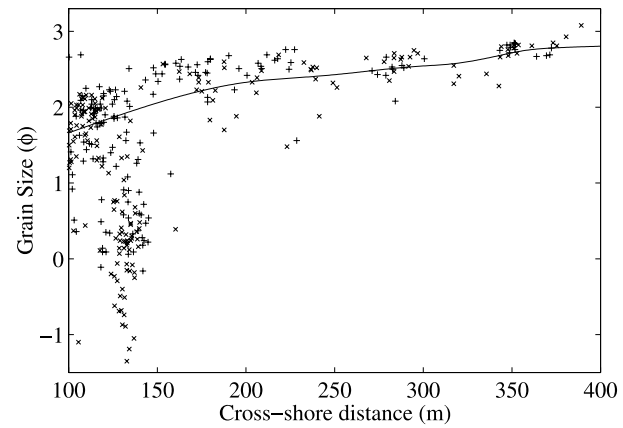

Figure 2. Sample median grain sizes observed by *Stauble and Cialone* [1997] during (+) August and (×) October versus cross-shore location. Solid curve marks grain sizes used for simulations. Here ϕ is the negative logarithm, base 2, of the grain diameter in millimeters.

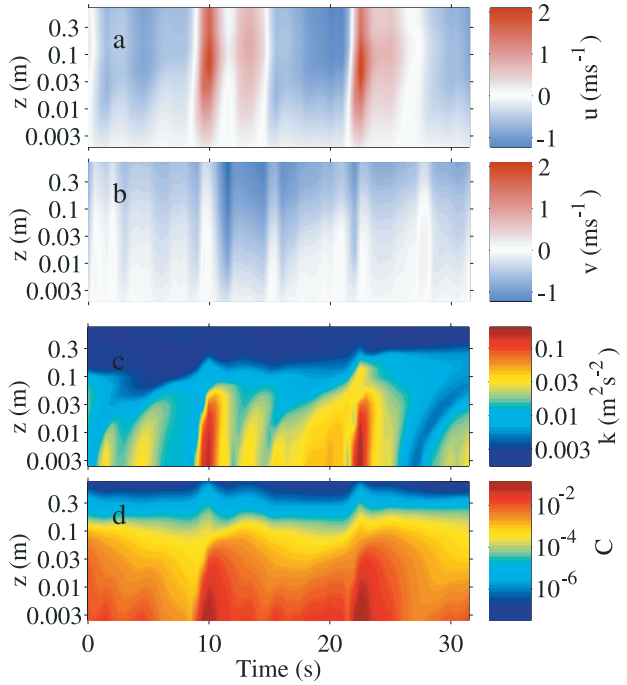

Figure 3. (a) Simulated cross-shore velocity, (b) longshore velocity, (c) turbulent energy, and (d) sediment concentration versus time and elevation above seabed for half a minute during 27 September.

spline through estimated q_1^* values. The depth change was then calculated from

$$\frac{\partial h^*}{\partial t^*} = \frac{1}{1-n}\frac{\partial \hat{q}_1^*}{\partial x_1^*}, \tag{20}$$

where the seabed porosity $n = 0.3$ [*Thornton et al.*, 1996]. We neglected downslope gravity-driven transport. The parameter α in equation (18) was chosen to minimize the error between predicted and observed erosion and accretion. Once chosen, this α value remained fixed for all cross-shore locations and all times (so the same α value was used for all three bar migration events considered below).

[31] Equation (20) relies on an assumption that the beach is longshore-uniform, so that the divergence of the longshore sediment flux is zero. *Ruessink et al.* [2001] found that the bathymetry at Duck was relatively longshore-uniform from 1 September to 11 October, and relatively nonuniform thereafter. We present results from only the interval 1 September to 11 October.

4. Predicted Sediment Transport and Beach Evolution

[32] Figure 3 shows velocity, turbulent energy, and sediment concentration fields predicted over the bar crest (cross-shore location 240 m) for half a minute during 27 September, when waves were moderately energetic (significant wave height $Hs = 0.77$ m in 8 m water depth). Velocities were dominated by waves, and velocity shear was mostly confined to a region within about 0.1 m of the bed (the wave boundary layer). Turbulence was most energetic

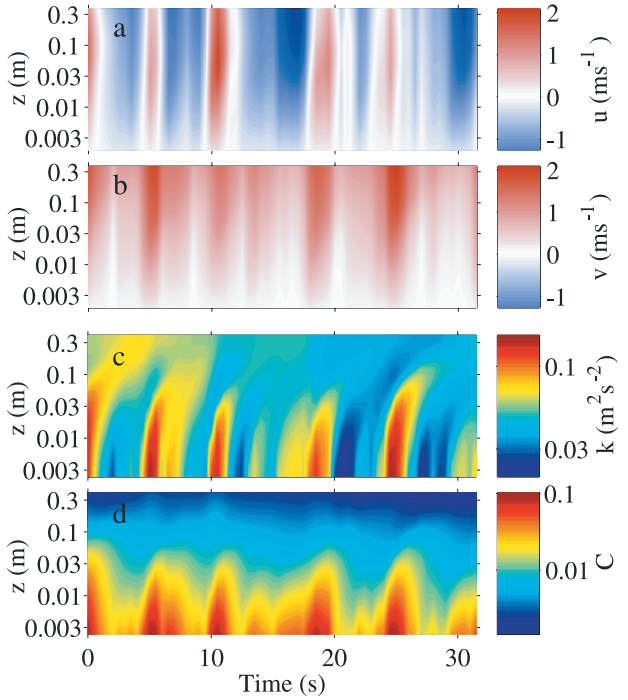

Figure 4. Similar to Figure 3, but for half a minute during 4 September.

in the wave boundary layer, where turbulent production (equation (A3)) was strong. Both turbulent energy and sediment concentration decreased very rapidly with distance above the wave boundary layer.

[33] Figure 4 shows velocity, turbulent energy, and sediment concentration fields predicted over the bar crest during a storm (Hs = 1.7 m) on 4 September. The cross-shore velocity was dominated by waves. There was a strong mean longshore current, whose shear extended above the wave boundary layer. This shear led to significant production of turbulence above the wave boundary layer. Consequently, turbulence intensities and sediment concentrations did not decay as rapidly with elevation in this case as they did on 27 September.

[34] The mean Eulerian sediment flux $\langle u_j^* \mathcal{C} \rangle$ equals the sum of the "current-generated flux" $\langle u_j^* \rangle \langle \mathcal{C} \rangle$ and the "wave-generated flux" $\langle (u_j^* - \langle u_j^* \rangle)\ (\mathcal{C} - \langle \mathcal{C} \rangle) \rangle$. Figure 5 shows vertical profiles of three-hour averaged current- and wave-generated fluxes. On 27 September, when waves were moderately energetic, the shoreward wave-generated flux exceeded the seaward current-generated flux, so sediment was transported shoreward (Figure 5a). The longshore flux was weak (Figure 5b). On 4 September, when mean currents were stronger, the seaward current-generated flux exceeded the shoreward wave-generated flux, so sediment was transported seaward (Figure 5c). The longshore flux was strong, and dominated by the current-generated flux (Figure 5d). Most of the wave-generated sediment flux was concentrated within the wave boundary layer whereas, on 4 September, the current-generated flux extended above the wave boundary boundary layer.

[35] We used our model to predict sediment transport at many cross-shore locations over six weeks. The results presented in Figures 3–5 constitute a very small part of the entire data set, and were chosen because sediment transport rates were large during 4 and 27 September. Nevertheless, many features of these results were typical of the larger data set, including the seaward current-generated transport, the shoreward wave-generated transport, and the confinement of most wave-generated transport to the wave boundary layer. *Conley and Beach* [2003] observed similar vertical profiles of sediment flux in the field. Concentration of wave-generated transport in the wave boundary layer was also observed in the laboratory by *van Rijn and Havinga* [1995].

[36] Figure 6a shows the depth-integrated shoreward sediment flux $\hat{q}_1^*$ as a function of time and cross-shore distance for most of the Duck94 experiment. The approximate bar crest location, calculated by interpolating observed bed elevations, is marked by a black curve. During much of the experiment (e.g., 10–20 September), the model predicted almost no sediment transport, and the bar was stationary. The bar moved seaward during the storms of 1–5 September and 2–4 October. On these occasions, the model predicted a maximum in seaward sediment transport over the sandbar, so the predicted sediment flux converged (diverged) on the seaward (shoreward) side of the bar. This cross-shore distribution of fluxes seems qualitatively consistent with the observed seaward bar migration, but quantitative calculations (presented below) show that only the first seaward bar migration was predicted successfully. The bar migrated shoreward during 22–27 September. Consistent with this

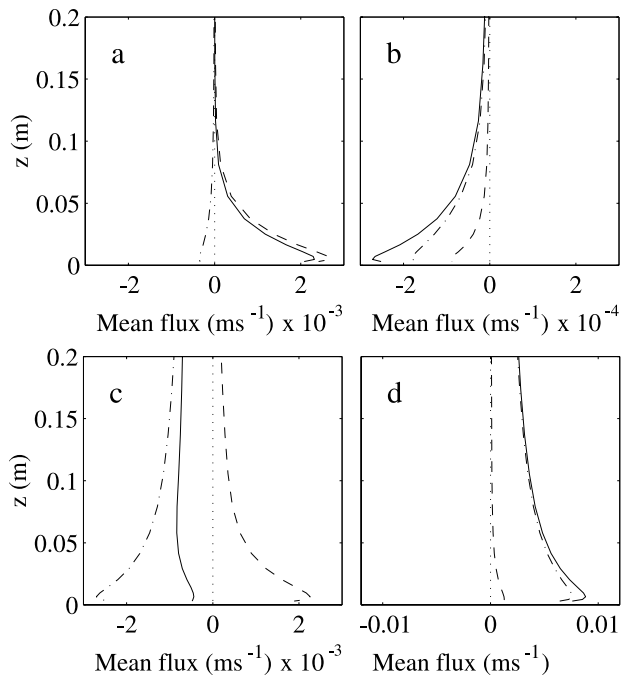

Figure 5. Vertical profiles of average (a and c) shoreward and (b and d) longshore Eulerian sediment flux for three hours during (Figures 5a and 5b) 27 September and (Figures 5c and 5d) 4 September. Solid lines, total flux; dashed lines, wave-generated flux; dash-dotted lines, current-generated flux; dotted lines mark zero flux.

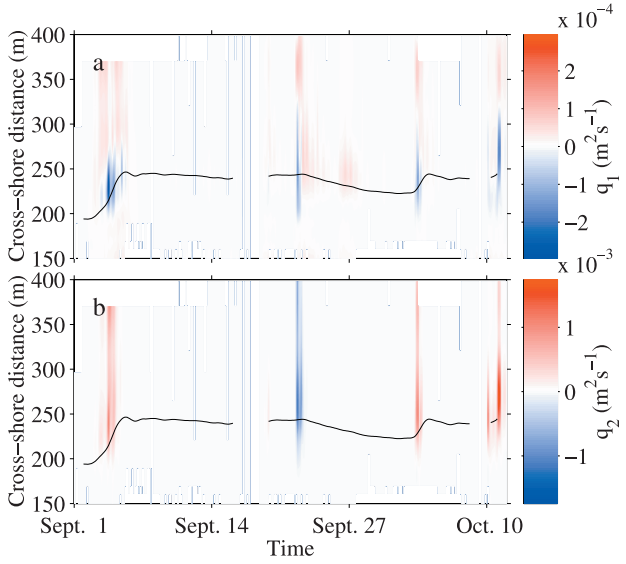

Figure 6. Simulated sediment flux (color) and estimated bar crest location (black curve) versus time and cross-shore location. (a) Shoreward flux. (b) Longshore flux.

observed bar migration, the model predicted a maximum in the shoreward sediment transport near the bar crest, with convergence (divergence) on the shoreward (seaward) side of the bar.

[37] During storms, when mean longshore currents were strong, the depth-integrated longshore sediment flux q_2^* was usually about 2–10 times larger than the cross-shore flux q_1^* (Figure 6). Consequently, the assumption $\partial q_2^*/\partial x_2^* \ll \partial q_1^*/\partial x_1^*$, required to derive equation (20), was valid only if the beach was extremely longshore uniform. The cross-shore-integrated longshore sediment flux $\int q_2^* dx_1^*$, calculated by trapezoidal integration of q_2^* predictions, ranged between -0.16 $m^3 s^{-1}$ and 0.14 $m^3 s^{-1}$. *Komar*

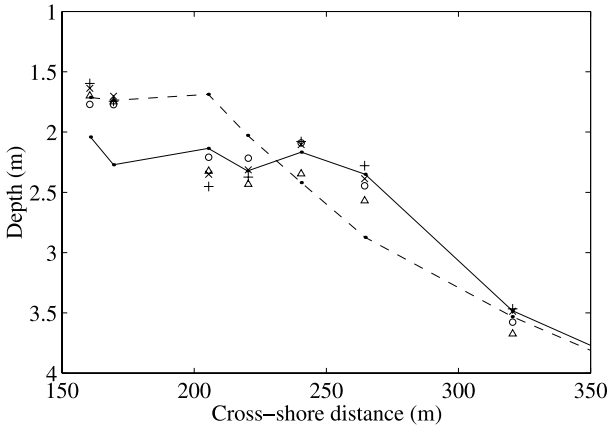

Figure 7. Observed and predicted water depth profiles. Dashed (solid) line represents observed profile at 7 pm on 1 September (7 pm, 5 September). Symbols represent predicted profiles for 5 September. Circles, advective boundary layer model; triangles, nonadvective boundary layer model; pluses, energetics model; crosses, combined energetics and acceleration model.

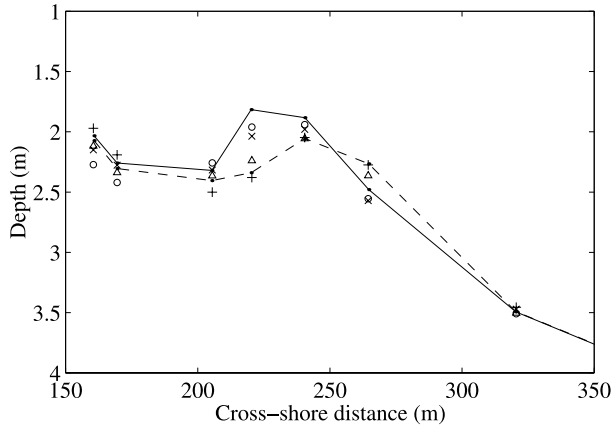

Figure 8. As Figure 7 but for period 22 September, 7 pm to 27 September, 7 pm.

and Inman [1970] suggested that the cross-shore-integrated longshore flux equals

$$Q_l = 0.77 \frac{\mathcal{E}_b \, Cg_b \sin\theta_b \cos\theta_b}{(\rho_s - \rho_w) g}, \tag{21}$$

where $\mathcal{E}_b$, Cg_b, and θ_b are respectively the energy density, group velocity, and propagation angle of waves at the breakpoint. To evaluate equation (21), we assumed that wave shoaling was linear and nondissipative between 8-m depth and the breakpoint, that waves broke when $Hs = 0.5h$, and that the wave angle in 8-m depth was given by the direction of the major principal axis of the covariance matrix between u_1 and u_2. The cross-shore-integrated longshore flux calculated by our model was correlated with, but smaller than, the flux predicted by equation (21) (by linear regression, $\int q_2^* dx_1^* = 0.43 Q_l$, with $r^2 = 0.62$). Our estimate of the total longshore sediment flux is expected to be an underestimate because, both onshore and offshore of the instrument array, the sediment flux could not be calculated and was omitted. The omission of the flux above z_t (equation (19)) might have caused further underestimation.

[38] Observed and predicted beach profile evolution are compared in Figures 7, 8, and 9. Offshore of 350 m, both predicted and observed changes in bed elevation were

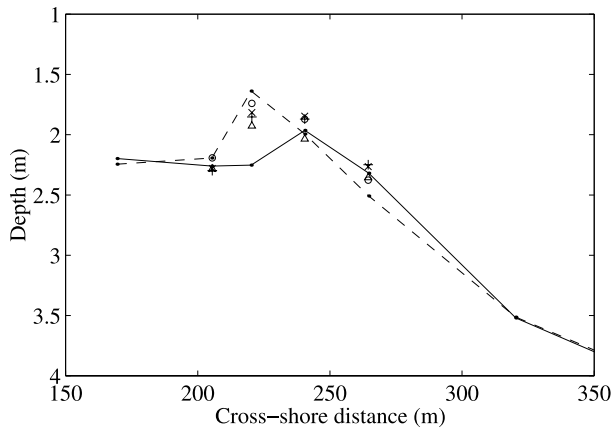

Figure 9. As Figure 7 but for period 2 October, 4 pm to 4 October, 4 pm.

Table 1. Model Parameters and Skill Scores

Model	Grain Size	z_0, $\times 10^{-3}$ m	β	α, $\times 10^{-3}$	Skill, 1–5 Sept.	Skill, 22–27 Sept.	Skill, 2–4 Oct.
Advective	variable	0.3	1	2.9	0.70	0.81	0.05
Advective	variable	1	1	1.6	0.73	0.80	0.13
Advective	variable	3	1	0.81	0.72	0.79	0.23
Advective	variable	1	1.5	0.15	0.70	0.76	0.03
Nonadvective	variable	1	1	1.6	0.55	0.37	0.64
Advective	constant	1	1	1.8	0.78	0.64	−0.04
Energetics	variable	—	—	—	0.62	−0.23	0.45
Energetics + acceleration	variable	—	—	—	0.65	0.80	0.34

small. Onshore of 150 m instruments emerged from the water at low tide, and no predictions of bed elevation change were made. Following *Gallagher et al.* [1998], we define the model skill over a given time interval as

$$S = 1 - \frac{\int_a^b (h_p - h_o)^2 \, dx}{\int_a^b (h_i - h_o)^2 \, dx}, \tag{22}$$

where h_p, h_o and h_i are respectively the predicted final, observed final, and observed initial depths, and a (b) is the most seaward (shoreward) location at which both sonar observations and model predictions are available. Integrals were calculated using the trapezoidal rule and known integrand values at the instrument locations. If profile evolution was predicted perfectly, then the skill would equal 1. If model predictions were more accurate (as measured by mean square error) than the baseline assumption of zero beach change, then the skill would be positive. If model predictions were less accurate than the zero-change assumption, then the skill would be negative. Model parameters and skill scores are summarized in the second row of Table 1.

[39] The fitted value of the calibration coefficient α (1.6×10^{-3}) was about two-thirds of the value suggested by *Smith and McLean* [1977]. This small discrepancy could be accounted for by an error in the assumed value of z_0 (see below), or by differences between the total stress (used in equation (15)) and the effective stress (used by Smith and McLean). Offshore of about 180 m, the erosion and seaward bar migration of 1–5 September was predicted successfully (circles, Figure 7). The simulated erosion and seaward bar migration were driven by a maximum in seaward current-generated transport over the bar crest. The model failed to predict the beach erosion observed onshore of 180 m. The shoreward bar migration of 22–27 September was predicted successfully (Figure 8). Erosion was predicted, but not observed, onshore of 180 m. The model failed to predict the seaward bar migration of 2–4 October (Figure 9).

[40] The true value of the roughness length z_0, and the stress exponent β (equation (18)), are unknown. The sensitivity of profile evolution predictions to these parameters was tested by rerunning the model with $z_0 = 3 \times 10^{-4}$ m, $z_0 = 3 \times 10^{-3}$ m, and $\beta = 1.5$. For each combination of parameters, a new value of α was chosen to optimise the predictions of beach profile evolution. Skill scores and best fit α values for these tests are given in Table 1. Model skill was fairly insensitive to z_0 and β. The best fit α value for $\beta = 1.5$ was about one tenth of the value that *van Rijn* [1984] found explained total scour rates observed during laboratory experiments. When van Rijn's coefficient was used, predicted sediment concentrations occasionally exceeded one. Therefore van Rijn's formula must be modified if it is to provide an accurate lower boundary condition for models of sediment suspension under energetic field conditions.

[41] Replacing the cross-shore variation in grain diameter shown in Figure 2 with a constant grain diameter of 2×10^{-4} m led to predictions of substantial erosion onshore of 180 m, but had little effect on predictions offshore of 180 m. This slightly increased the model skill for 1–5 September, when the seabed onshore of 180 m eroded, but slightly decreased the model skill for 22–27 September, when the seabed onshore of 180 m accreted (Table 1).

[42] Predictions of seabed evolution made using previously published models are also plotted in Figures 7, 8, and 9. Predictions calculated using *Bailard*'s [1981] energetics model are marked by pluses. Predictions calculated using *Hoefel and Elgar*'s [2003] acceleration-based modification of Bailard's model are marked by crosses. The sediment fluxes predicted by the various models are com-

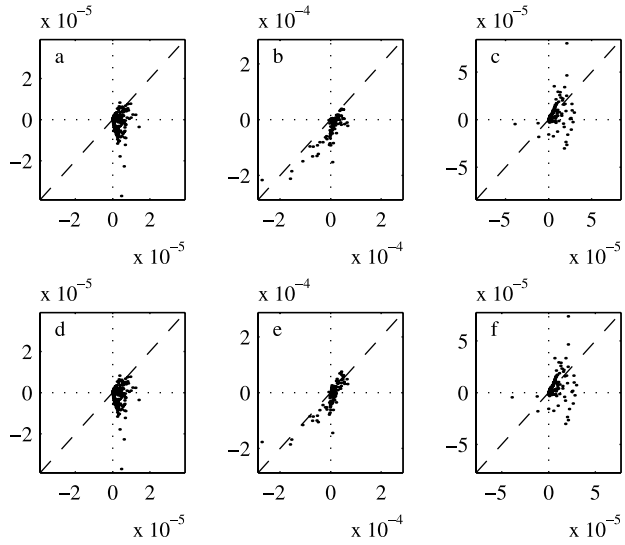

Figure 10. Three-hour averaged shoreward sediment fluxes ($m^2 s^{-1}$) predicted by advective boundary layer model (x axes) versus fluxes predicted by (a, b, and c) energetics, and (d, e, and f) acceleration-based models. Predictions from cross-shore locations (Figures 10a and 10d) 170 m, (Figures 10b and 10e) 240 m, (Figures 10c and 10f) 320 m. The r^2 values for Figures 10a–10f are 0.03, 0.48, 0.17, 0.03, 0.62, and 0.17, respectively.

pared in Figure 10, and skill scores are recorded in the last two rows of Table 1. We used the formulas and parameters given by *Gallagher et al.* [1998] and *Hoefel and Elgar* [2003], with the following exceptions:

[43] 1. Sediment fall velocity was calculated using the grain diameters marked by the solid curve in Figure 2.

[44] 2. Errors in current meter orientations were corrected, as described in section 3.

[45] 3. A weakly smoothing spline was used to derive continuous cross-shore profiles of sediment flux, from which flux divergences were calculated.

[46] Both energetics- and acceleration-based models successfully predicted the seaward bar migration of 1–5 September (Figure 7 and Table 1). This seaward bar migration was caused by large seaward sediment fluxes over the bar crest. The large seaward fluxes over the bar crest predicted by enegertics- and acceleration-based models were similar to the large seaward fluxes predicted by our boundary layer model (well correlated negative fluxes in Figures 10b and 10e). During 22–27 September, the energetics-based model did not predict the shoreward flux over the bar crest predicted by our model (Figure 10b), and failed to predict shoreward bar migration (Figure 8 and Table 1; see also *Gallagher et al.* [1998]). In contrast, the acceleration-based model predicted this shoreward flux (Figure 10e), and successfully predicted shoreward bar migration (Figure 8 and Table 1; see also *Hoefel and Elgar* [2003]). Energetics- and acceleration-based models both failed to predict the seaward bar migration of 2–4 October, as well as the profile evolution onshore of 180 m. Both onshore and offshore of the bar, the fluxes predicted by the boundary layer model differed from the fluxes predicted by energetics- and acceleration-based models (Figures 10a, 10c, 10d, and 10f), although all predicted fluxes were relatively small.

[47] Energetics- and acceleration-based predictions are equal (different) when the magnitude of

$$a_{\text{spike}} = \frac{\left\langle \left(\partial \breve{u}_1^*/\partial t^*\right)^3 \right\rangle}{\left\langle \left(\partial \breve{u}_1^*/\partial t^*\right)^2 \right\rangle} \tag{23}$$

is less (greater) than $a_{\text{crit}} = 0.2\ \text{ms}^{-2}$, where $\breve{u}_1^*$ is low-pass filtered u_1^*. Following *Hoefel and Elgar* [2003], we used a low-pass cutoff frequency of 0.5 Hz. This cutoff excludes from calculations of a_{spike} the very sudden shoreward accelerations that coincide with the passage of bores very near the shore. The cutoff also excludes any acceleration skewness that might arise from high frequency turbulence. Filtering was required to prevent incorrect predictions of rapid erosion shoreward of 180 m. At the cross-shore location 170 m (240 m), a_{crit} was exceeded during only one (three) 3-hour time series between 1 September and 11 October. Consequently, energetics- and acceleration-based models predicted almost identical fluxes at these locations (so Figures 10a and 10c are almost indistinguishable from Figures 10d and 10f).

[48] All the models considered above failed to predict the seaward bar migration of 2–4 October. We do not know why, although the predicted longshore sediment flux was about 5–10 times larger than the cross-shore flux during 2–4 October (Figure 6), so the longshore flux divergence, neglected in equation (19), might have been important.

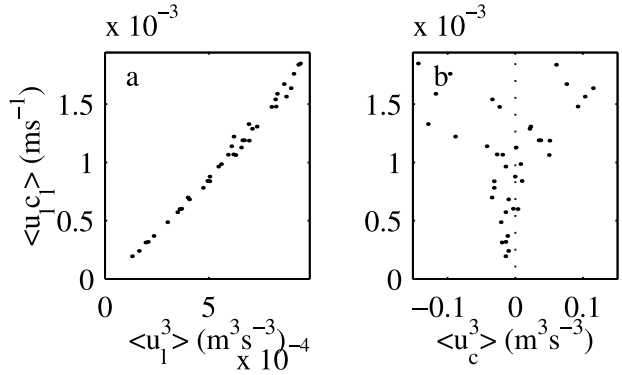

Figure 11. Near-bed shoreward sediment flux $\langle u_l \mathcal{C}_l \rangle$, versus third moment of (a) near-bed velocity $\langle u_l^3 \rangle$ and (b) free-stream velocity $\langle u_c^3 \rangle$. Data from bar crest (cross-shore location 205 m), with one data point for every three hours of 22–27 September.

5. Mechanisms Responsible for Predicted Transport

5.1. Skewness and Asymmetry

[49] Much suspended sediment is transported within the wave boundary layer (Figure 5). Next, we present a simple relationship between the suspended sediment flux very near the bed and the colocated water velocity. Pickup of sediment from the seabed scaled with the bed stress (equation (18)), which in turn scaled with the square of the near-bed velocity u_l. Making the orthodox assumption that the near-bed sediment concentration adjusted instantaneously to the near-bed flow [*Fredsoe and Deigaard*, 1992; *Davies et al.*, 2002], we expect the near-bed concentration to scale with u_l^2, and the near-bed flux to scale with u_l^3. Figure 11a confirms that, during a period when mean currents were weak, the near-bed suspended sediment flux $\langle u_l \mathcal{C}_l \rangle$, where u_l and $\mathcal{C}_l$ are respectively shoreward velocity and sediment concentration 2 mm above the bed, was indeed correlated strongly ($r^2 = 0.997$) with $\langle u_l^3 \rangle$. In contrast, $\langle u_l \mathcal{C}_l \rangle$ was correlated poorly ($r^2 = 0.008$) with the third moment of the free-stream velocity u_c (measured by a current meter about 0.7 m above the bed, Figure 11b). Motivated by this result, we will examine the relationship between free-stream and near-bed velocities, with particular emphasis on near-bed velocity skewness.

[50] Figure 12 shows the cross-spectral relationship between near-bed and free-stream velocities over the bar crest for three hours on 27 September. Despite the potentially strong nonlinearity of the turbulence closure model, near-bed and free-stream velocities were highly coherent over the energetic part of the spectrum (0.05–0.25 Hz). The near bed velocity led the free-stream velocity by 25–30 degrees. If momentum fluxes are negligible and the eddy viscosity equals $\kappa z^* (\tau_0/\rho_w^*)^{1/2}$, where τ_0 is a typical (time-independent) magnitude of the bed shear stress, then an analytic model predicts the transfer function between free-stream and near-bed velocities [e.g., *Mei*, 1989, section 8.7.1]. Over the energetic part of the spectrum, analytic and numerical models predicted similar gain and phase between

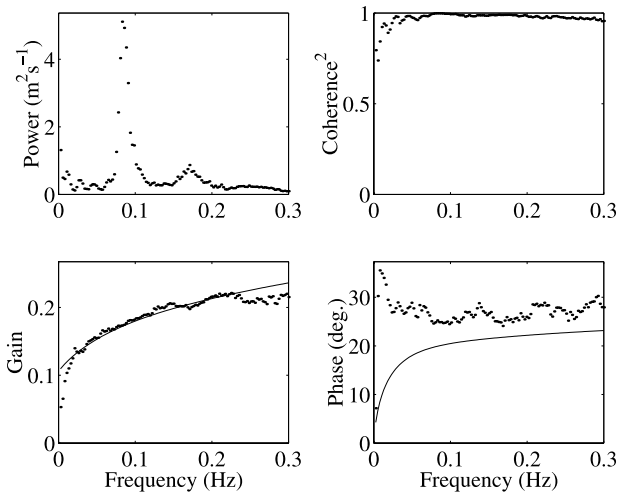

Figure 12. Power spectrum of free-stream cross-shore velocity, together with coherence-squared, gain, and phase between free-stream and near-bed velocity. The positive phase, and gain less than 1, indicate that near-bed velocity fluctuations lead, and are smaller than, free-stream fluctuations. Dots indicate values from numerical simulation of 3 hours on 27 September. Lines indicate analytic approximation [*Mei*, 1989, section 8.7.1].

near-bed and free stream velocities, although the analytic model predicted a slightly smaller phase (Figure 12). At low frequencies (<0.05 Hz), analytic and numerical models predicted different transfer functions, and the coherence between free-stream and near-bed velocities declined. Phase shifts of 15–40 degrees between near-bed and free-stream velocities have been observed in the laboratory [*Johnsson and Carlsen*, 1976] and in the field [*Trowbridge and Agrawal*, 1995].

[51] During the period considered in Figure 11 (22–27 September), mean currents were weak, so the dimensional near-bed skewness $S_l = \langle (u_l - \langle u_l \rangle)^3 \rangle$ was a large component of the third moment of the near bed velocity. Owing to the boundary layer phase shift described above, the near-bed skewness depended on both the dimensional skewness $S_c = \langle (u_c - \langle u_c \rangle)^3 \rangle$ and asymmetry $A_c = -\langle (H[u_c] - \langle H[u_c] \rangle)^3 \rangle$ of the free-stream velocity (where $H[\cdot]$ denotes the Hilbert transform). By linear regression, using all 3-hour time series over the bar crest (cross-shore position 205 m) from 1 September to 11 October,

$$S_l \approx 9.6 \times 10^{-3}(S_c + 0.39A_c), \tag{24}$$

with an r^2 of 0.99.

[52] To see why the near-bed skewness depended on the free-stream asymmetry, first note that the near-bed dimensional skewness

$$S_l = 12 \int_{\omega_1=0}^{\infty} \int_{\omega_2=0}^{\omega_1} \Re[\Phi_l(\omega_1, \omega_2)]\, d\omega_2\, d\omega_1, \tag{25}$$

and the near-bed dimensional asymmetry

$$A_l = -12 \int_{\omega_1=0}^{\infty} \int_{\omega_2=0}^{\omega_1} \Im[\Phi_l(\omega_1, \omega_2)]\, d\omega_2\, d\omega_1, \tag{26}$$

where the bispectral density

$$\Phi_l(\omega_1, \omega_2) = \frac{E[dZ_l(\omega_1)\, dZ_l(\omega_2)\, \mathrm{conj}\{dZ_l(\omega_1 + \omega_2)\}]}{d\omega_1\, d\omega_2}, \tag{27}$$

$dZ_l(\omega)$ is the infinitesimal complex amplitude of the frequency-ω fluctuation in u_l, $d\omega$ is the infinitesimal frequency resolution, and $\Re[\cdot]$, $\Im[\cdot]$, conj$\{\cdot\}$ and $E[\cdot]$ respectively denote the real part, the imaginary part, the complex conjugate, and the expected value [*Priestley*, 1988]. Since near-bed and free-stream velocities were very coherent,

$$dZ_l(\omega) \approx 0.2 e^{0.44i} dZ_c(\omega), \tag{28}$$

where $dZ_c(\omega)$ is the complex amplitude of the frequency-ω fluctuation in u_c, and the frequency-dependent phase and gain have respectively been approximated by the constants 0.44 radians (25 degrees) and 0.2 (c.f. Figure 12). From equations (27) and (28)

$$\Phi_l(\omega_1, \omega_2) \approx 8 \times 10^{-3} e^{0.44i} \Phi_c(\omega_1, \omega_2), \tag{29}$$

where $\Phi_c(\omega_1, \omega_2)$ is the free-stream bispectral density. From equations (25) and (29)

$$S_l \approx 8 \times 10^{-3} \times 12 \Big\{ \cos(0.44) \int_{\omega_1=0}^{\infty} \int_{\omega_2=0}^{\omega_1} \Re[\Phi_c(\omega_1, \omega_2)]\, d\omega_2\, d\omega_1 - \sin(0.44) \cdot \int_{\omega_1=0}^{\infty} \int_{\omega_2=0}^{\omega_1} \Im[\Phi_c(\omega_1, \omega_2)]\, d\omega_2\, d\omega_1 \Big\}, \tag{30}$$

$$\Rightarrow S_l \approx 7.3 \times 10^{-3}(S_c + 0.47A_c), \tag{31}$$

in rough agreement with equation (24).

[53] Qualitatively, the conversion of asymmetry to skewness results from the frequency-independent shift in phase (equation (28)), which corresponds to a frequency-dependent shift in the timing of the Fourier components. The change in the relative timing of the Fourier components systematically changes the shapes of the velocity fluctuations.

[54] The near-bed sediment flux depended on the near-bed skewness (Figure 11), which in turn depended on the free-stream asymmetry (equation (24)). Therefore the near-bed suspended sediment flux depended on the free-stream asymmetry. *Nielsen* [1992] suggested that the bedload transport scales with $\tau^{3/2}$ (which in turn scales with u_l^3), and introduced a boundary layer phase shift to predict nonzero mean transport under asymmetric waves. Qualitatively, *Nielsen*'s [1992] mechanism for asymmetry-dependent bedload transport is similar to the mechanism discussed above for asymmetry-dependent near-bed suspended load transport. Quantitatively, the gain and phase used by *Nielsen* [1992] differ from the gain and phase predicted here.

[55] Since the free-stream asymmetry tends to have a maximum over the bar [*Elgar et al.*, 2001], the asymmetry-dependent sediment transport discussed above might drive shoreward bar migration. However, the near-bed flux is only part of the total depth-integrated flux, and the dependence

of the depth-integrated flux on the water velocity was complex. *Bagnold* [1966], *Bailard* [1981], and *Bowen* [1981] suggested that the depth-integrated suspended sediment flux over a flat seabed is proportional to $\langle |u_c|^3 u_c \rangle$. During 22–27 September, the depth-integrated flux was correlated poorly ($r^2 = 0.24$) with $\langle |u_c|^3 u_c \rangle$. However, there was a strong correlation ($r^2 = 0.97$) between the depth-integrated flux and $\langle |u_l|^3 u_l \rangle$. Interpretation of this result is complicated by the Stokes drift contribution to the depth-integrated flux, which is discussed below (near the bed, the skew flux, also discussed below, is very small. Consequently, the Stokes drift does not complicate interpretation of the near-bed flux). Furthermore, for the model presented here, asymmetry-dependent transport alone does not lead to successful predictions of observed shoreward bar migration (below we show that momentum fluxes and the Stokes drift are also required). Finally, the correlation between $\langle |u_l|^3 u_l \rangle$ and the depth-integrated flux was poor when mean currents were strong (e.g., $r^2 = 0.0095$ for the period 1–5 September).

5.2. Momentum Fluxes and the Stokes Drift

[56] The importance of the nonlinear advective terms (the second and third terms of equations (10), (13), (A1), and (A2)) was assessed by rerunning the model with the advective terms switched off (triangles, Figures 7–9, and skill scores on the fifth row of Table 1). The shoreward bar migration of 22–27 September was not predicted when nonlinear advective terms were neglected. The amount by which the shoreward sediment flux decreased when all advective terms were switched off will be called the total advectively induced flux. To isolate the processes responsible for this flux, we ran the model repeatedly, for each run switching off the advective terms in only one of equations (10), (13), (A1), and (A2). Removal of advective terms from equation (A1) had little effect on sediment transport predictions (changes were usually <10% of the total advectively induced flux). Removal of advective terms from equation (A2) also had little effect. When waves were (were not) very energetic, removal of advective terms from the momentum equation (10) accounted for slightly less (more) than half of the total advectively induced flux. Therefore momentum fluxes encouraged shoreward bar migration, as previously suggested by *Trowbridge and Young* [1989]. When waves were (were not) very energetic, removal of advective terms from the sediment conservation equation (13) accounted for slightly more (less) than half of the total advectively induced flux. The advective terms of equation (13) were not included in *Trowbridge and Young*'s [1989] bedload transport model.

[57] The advective terms in the sediment conservation equation (13) introduce to our Eulerian model sediment transport by the Stokes drift. *Middleton and Loder* [1989] discuss, in general terms, the Eulerian view of tracer advection by the Stokes drift. We will present a simpler, but less general, discussion. Advection of the mean sediment concentration $\langle \mathcal{C} \rangle$ by the fluctuating vertical displacement $Z^* = \int^{t^*} w^* dt'^*$ generates a concentration fluctuation $\hat{\mathcal{C}}$ roughly equal to $-Z^* \partial \langle \mathcal{C} \rangle / \partial z^*$. In a statistically steady wave field, the resulting mean sediment flux

$$F_s^* = \left\langle u_1^* \hat{\mathcal{C}} \right\rangle = -\langle u_1^* Z^* \rangle \partial \langle \mathcal{C} \rangle / \partial z^* \tag{32}$$

is called a skew flux. This skew flux can be expressed in terms of the Stokes drift

$$u_{ST}^* = \left\langle Z^* \frac{\partial u_1^*}{\partial z^*} \right\rangle + \left\langle X^* \frac{\partial u_1^*}{\partial x^*} \right\rangle, \tag{33}$$

where $X^* = \int^{t^*} u_1^* dt'^*$ is the shoreward particle displacement. To show this, we first establish that

$$u_{ST}^* = \frac{\partial \langle u_1^* Z^* \rangle}{\partial z^*}. \tag{34}$$

From equation (33),

$$u_{ST}^* = \frac{\partial \langle u_1^* Z^* \rangle}{\partial z^*} + \frac{\partial \langle u_1^* X^* \rangle}{\partial x^*} - \left\langle u_1^* \left(\frac{\partial X^*}{\partial x^*} + \frac{\partial Z^*}{\partial z^*} \right) \right\rangle. \tag{35}$$

The terms in parentheses are the time integral of the divergence and equal zero. Now noting that $\langle u_1^* X^* \rangle = \langle \partial X^{*2} / \partial t^* \rangle / 2 = 0$ (by stationarity) yields equation (34).

[58] Now from equation (32)

$$F_s^* = -\frac{\partial \langle u_1^* Z^* \rangle \langle \mathcal{C} \rangle}{\partial z^*} + \langle \mathcal{C} \rangle \frac{\partial \langle u_1^* Z^* \rangle}{\partial z^*}. \tag{36}$$

From equations (34) and (36)

$$F_s^* = \langle \mathcal{C} \rangle u_{ST}^* - \frac{\partial \langle u_1^* Z^* \rangle \langle \mathcal{C} \rangle}{\partial z^*}. \tag{37}$$

The first term on the right of equation (37) represents the advection of sediment by the Stokes drift. The second term often is nonzero, and complicates the interpretation of F_s^*. Nevertheless, the vertically integrated flux

$$\int_{z^*=z_l}^{z_t} F_s^* \, dz^* = \int_{z^*=z_l}^{z_t} \langle \mathcal{C} \rangle u_{ST}^* \, dz^* - \langle \mathcal{C} \rangle \langle u_1^* Z^* \rangle \big|_{z^*=z_t} + \langle \mathcal{C} \rangle \langle u_1^* Z^* \rangle \big|_{z^*=z_l} \tag{38}$$

has a simple interpretation [see also *van Hardenberg et al.*, 1991]. Since $\langle \mathcal{C} \rangle$ is usually very small at z_t, and Z^* is very small ($O[(z_l - z_0)^2]$) for z_l close to z_0,

$$\int_{z=z_l}^{z_t} F_s^* \, dz \approx \int_{z=z_l}^{z_t} \langle \mathcal{C} \rangle u_{ST}^* \, dz. \tag{39}$$

Therefore nonlinear advection of the mean concentration profile introduces a depth-integrated sediment flux equal to the depth-integrated advection of sediment by the Stokes drift. The above analysis is highly simplified, partly because advection of the mean concentration profile is only one component of the total advection (further fluxes arise from advection of the fluctuating concentration profile). Nevertheless, the Stokes drift transport, calculated from the right of equation (39), accounted for most of the additional transport induced by nonlinear sediment advection (Figure 13).

6. Conclusions

[59] The sandbar migration observed during the Duck94 field experiment has been simulated by combining water velocity measurements with a model of water and sediment

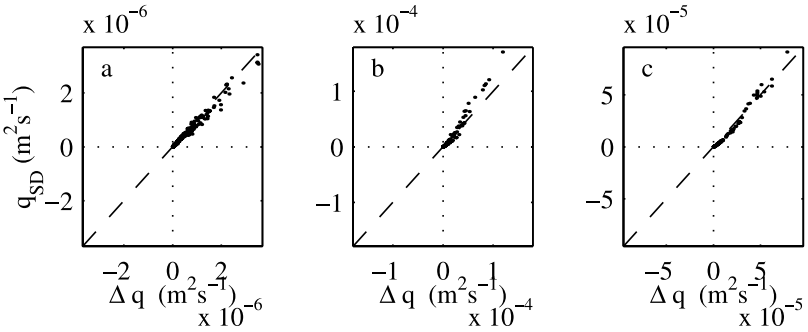

Figure 13. Three-hour averaged shoreward sediment advection by Stokes drift, q_{SD}, versus the sediment flux induced by nonlinear sediment advection, $\Delta q = q_1^* - q_1^{*\prime}$, where q_1^* is the depth-integrated sediment flux predicted by the fully advective model, and $q_1^{*\prime}$ is the flux predicted by a model that included all advective terms except those in equation (13). Predictions are from cross-shore locations (a) 170 m, (b) 240 m, and (c) 320 m.

motion in the bottom boundary layer. The model successfully predicted one shoreward bar migration event and one seaward bar migration event. The model failed to predict a second seaward bar migration event. Predictions of depth changes onshore of the trough were poor. Therefore the model presented here had similar skill to the model previously presented by *Hoefel and Elgar* [2003]. The model presented here has the disadvantage that it is much less computationally efficient than the model of *Hoefel and Elgar* [2003]. However, because the model presented here is based on solutions to relatively well-established momentum and mass conservation equations, it can be used to examine the physical processes responsible for simulated bar migration.

[60] The shoreward bar migration event is particularly interesting, because it is not predicted by the standard energetics model of *Bailard* [1981]. Horizontal pressure forces on sediment particles might be important to shoreward bar migration [*Drake and Calantoni*, 2001]. The horizontal pressure force on sediment particles was excluded from the model derived here, so the horizontal pressure gradient influenced predictions only inasmuch as it determined the water velocity. Nevertheless, shoreward sandbar migration was predicted successfully. Further research will be required to determine the importance to nearshore sediment transport of the horizontal pressure force on sediment particles.

[61] Seaward Eulerian mean currents carried suspended sediment seaward. A positive covariance between shoreward velocity and suspended sediment concentration led to shoreward transport, and was mostly concentrated within the wave boundary layer.

[62] The predicted water velocity within the wave boundary layer, where most shoreward transport occurred, differed from the free-stream velocity. When mean currents were weak, the suspended sediment flux very near (2 mm above) the bed was correlated strongly with the third moment of the near-bed cross-shore velocity, but was correlated poorly with the third moment of the free-stream velocity. Owing to a phase shift of about 25 degrees between free-stream and near-bed velocities, the third moment of the near-bed velocity depended on the asymmetry of the free-stream velocity. This led to asymmetry-dependence of near-bed suspended sediment transport, qualitatively similar to the asymmetry-dependence of bedload transport suggested by *Nielsen* [1992]. Quantitatively, the gain and phase predicted here differed from those used by *Nielsen* [1992].

[63] Since the asymmetry of the free-stream velocity often has a local maximum over the bar crest, the above mechanism for asymmetry-dependent transport might encourage shoreward bar migration. However, according to our model, this mechanism alone was not sufficient to explain the observed shoreward bar migration. Instead, nonlinear advection was required to predict shoreward bar migration. A wave-generated flux of shoreward momentum into the wave boundary layer, and the resulting boundary layer streaming, contributed to shoreward bar migration, as previously suggested by *Trowbridge and Young* [1989]. A further shoreward flux, due to nonlinear advection of suspended sediment, also contributed to shoreward bar migration. Most of this last flux was due to advection of sediment by the Stokes drift.

[64] The cross-shore-integrated longshore sediment flux predicted by our model was correlated with ($r^2 = 0.62$), but smaller than (about half) the longshore flux predicted by *Komar and Inman*'s [1970] empirical formula.

[65] Our model neglects many processes that might be important to sediment transport in the field, including bedload transport, downslope gravity-driven transport, injection of turbulence by breaking waves, and the spatial variations in bottom roughness that might arise from spatially varying bedforms. Further field observations will be required to determine the importance of these neglected processes.

Appendix A: Turbulence Closure

[66] Consistent with the approximations outlined in section 2.1, the k-ϵ equations are [c.f. *Pope*, 2000, equations 10.35, 10.40, and 10.53]

$$\frac{\partial k^*}{\partial t^*} - \frac{1}{c_0}\frac{\partial u_1^* k^*}{\partial t^*} + \frac{\partial w^* k^*}{\partial z^*} = \frac{\partial}{\partial z^*}\left(\nu^* \frac{\partial k^*}{\partial z^*}\right) + P^* - \epsilon^*, \quad \text{(A1)}$$

$$\frac{\partial \epsilon^*}{\partial t^*} - \frac{1}{c_0}\frac{\partial u_1^* \epsilon^*}{\partial t^*} + \frac{\partial w^* \epsilon^*}{\partial z^*} = \frac{\partial}{\partial z^*}\left(\frac{\nu^*}{1.3}\frac{\partial \epsilon^*}{\partial z^*}\right) + 1.44\frac{P^* \epsilon^*}{k^*} - 1.92\frac{(\epsilon^*)^2}{k^*}, \quad \text{(A2)}$$

where k^* and ϵ^* are the dimensional turbulent energy and dimensional dissipation respectively,

$$P^* = \nu^* \left[\left(\frac{\partial u^*}{\partial z^*} \right)^2 + \left(\frac{\partial v^*}{\partial z^*} \right)^2 \right] \tag{A3}$$

is the production of turbulent energy and

$$\nu^* = 0.09 \frac{(k^*)^2}{\epsilon^*}. \tag{A4}$$

[67] In a constant stress layer,

$$\frac{\partial k^*}{\partial z^*} = 0 \tag{A5}$$

and

$$\frac{\partial \epsilon^*}{\partial z^*} = -\frac{\epsilon^*}{z^*}. \tag{A6}$$

We require that equations (A5) and (A6) hold at the upper and lower boundaries of the numerical grid.

Appendix B: Calculation of Pressure Gradients

[68] Under assumption (12), the leading-order momentum equation

$$\frac{\partial u_j}{\partial t} + \frac{\partial p}{\partial x_j} = \frac{\partial}{\partial z} \left(\nu \frac{\partial u_j}{\partial z} \right), \tag{B1}$$

gives the expression for the leading-order pressure gradient $\partial p/\partial x_j = -\partial (u_j)_c/\partial t$, where $(u_j)_c$ is the velocity measured by the current meter. This pressure gradient was substituted into equation (B1), which was then solved for the vertical profile of u_j, accurate to leading order, with the upper boundary condition $u_j|_{z=z_c} = (u_j)_c$. Substitution of this velocity profile into equation (11), and subsequent vertical integration, gave a leading-order estimate of w. Substituting this w, together with the calculated u_j, into equation (10) and applying equation (12) yielded a second-order accurate estimate of the pressure gradient (evaluated half a grid point below the upper boundary. Calculation of the second-order-accurate pressure gradient at the upper boundary, using a noncentered finite difference to calculate $\partial w u_j/\partial z$, did not significantly change model results). Finally, this second-order accurate pressure gradient was substituted into equation (10) to calculate the velocity profile to second order. This procedure was repeated every time step. A constant viscosity version of this model successfully reproduced the analytic boundary layer streaming solution of *Longuet-Higgins* [1953].

[69] **Acknowledgments.** This research was funded by the Office of Naval Research's (ONR's) Coastal Dynamics Program under grant N00014-02-1-0100, and by the National Oceanographic Partnership Program (NOPP) through ONR grant N00014-99-1-1051. The Duck94 instrument array was deployed and maintained by staff from the Scripps Institution of Oceanography's Center for Coastal Studies. Principal investigators were Steve Elgar and R. T. Guza. T. H. C. Herbers, B. Raubenheimer and Edith L. Gallagher helped collect and process the data. The staff of the Field Research Facility of the U.S. Army Engineers Waterways Experiment Station's Coastal Engineering Research Center provided logistical support during the Duck94 experiment. We thank Steve Elgar for providing the data, Thomas H. C. Herbers for providing corrections to current meter orientation errors, Fernanda Hoefel for discussing mechanisms for shoreward sandbar migration, and Edith L. Gallagher for providing information about sand grains sizes during Duck94.

References

Bagnold, R. (1966), An approach to the sediment transport problem from general physics, *U.S. Geol. Surv. Prof. Pap., 422-I*, Reston, Va.

Bailard, J. A. (1981), An energetics total load sediment transport model for a plane sloping beach, *J. Geophys. Res.*, *86*, 10,938–10,964.

Bowen, A. (1981), Simple models of nearshore sedimentation: Beach profiles and longshore bars, *Coastline Can.*, *80-10*, 1–11.

Conley, D. C., and R. A. Beach (2003), Cross-shore sediment transport partitioning in the nearshore during a storm event, *J. Geophys. Res.*, *108*(C3), 3065, doi:10.1029/2001JC001230.

Davies, A., L. van Rijn, J. Damgaard, J. van de Graaff, and J. Ribberink (2002), Intercomparison of research and practical sand transport models, *Coastal Eng.*, *46*, 1–23.

Deigaard, R., and J. Fredsøe (1989), Shear stress distribution in dissipative water waves, *Coastal Eng.*, *13*, 357–378.

Deigaard, R., J. B. Jakobsen, and J. Fredsøe (1999), Net sediment transport under wave groups and bound long waves, *J. Geophys. Res.*, *104*, 13,559–13,575.

Drake, T. G., and J. Calantoni (2001), Discrete particle model for sheet flow sediment transport in the nearshore, *J. Geophys. Res.*, *106*, 19,859–19,868.

Elgar, S. (1987), Relationships involving third moments and bispectra of a harmonic process, *IEEE Transactions Acoust. Speech Signal Process.*, *12*, 1725–1726.

Elgar, S., R. Guza, B. Raubenheimer, T. Herbers, and E. L. Gallagher (1997), Spectral evolution of shoaling and breaking waves on a barred beach, *J. Geophys. Res.*, *102*, 15,797–15,805.

Elgar, S., E. L. Gallagher, and R. Guza (2001), Nearshore sandbar migration, *J. Geophys. Res.*, *106*, 11,623–11,627.

Feddersen, F., E. Gallagher, R. Guza, and S. Elgar (2003), The drag coefficient, bottom roughness, and wave breaking in the nearshore, *Coastal Eng.*, *48*, 189–195.

Fredsoe, J., and R. Deigaard (1992), *Mechanics of Coastal Sediment Transport*, World Sci., Tokyo.

Gallagher, E., W. Boyd, S. Elgar, R. Guza, and B. Woodward (1996), Performance of a sonar altimeter in the nearshore, *Mar. Geol.*, *133*, 241–248.

Gallagher, E. L., S. Elgar, and R. Guza (1998), Observations of sand bar evolution on a natural beach, *J. Geophys. Res.*, *103*, 3203–3215.

Gallagher, E. L., E. B. Thornton, and T. P. Stanton (2003), Sand bed roughness in the nearshore, *J. Geophys. Res.*, *108*(C2), 3039, doi:10.1029/2001JC001081.

Gibbs, R., M. Mathews, and D. Link (1971), The relationship between sphere size and settling velocity, *J. Sediment. Petrol.*, *41*, 7–18.

Herbers, T., and M. Burton (1997), Nonlinear shoaling of directionally spread waves on a beach, *J. Geophys. Res.*, *102*, 21,101–21,114.

Herbers, T., S. Elgar, and R. Guza (1999), Directional spreading of waves in the nearshore, *J. Geophys. Res.*, *104*, 7683–7693.

Hoefel, F., and S. Elgar (2003), Wave-induced sediment transport and sandbar migration, *Science*, *299*, 1885–1887.

Holmedal, L. E., D. Myrhaug, and H. Rue (2003), The sea bed boundary layer under random waves plus current, *Continent. Shelf Res.*, *23*, 717–750.

Janssen, C. M., W. N. Hassan, R. V. D. Wal, and J. S. Ribberink (1998), Grain-size influence on sand transport mechanisms, in *Coastal Dynamics '97*, pp. 58–67, Am. Soc. Civ. Eng., Reston, Va.

Johnsson, I. G., and N. A. Carlsen (1976), Experimental and theoretical investigations in an oscillatory turbulent boundary layer, *J. Hydraul. Res.*, *14*, 45–60.

Komar, P. D., and D. L. Inman (1970), Longshore sand transport on beaches, *J. Geophys. Res.*, *75*, 5914–5927.

Lee, G., and W. Birkemeier (1993), Beach and nearshore survey data: 1985–1991, CERC field research facility, in *Tech. Rep. CERC-93-3*, U.S. Army Corps of Eng., Waterw. Exp. Stn., Vicksburg, Miss.

Longuet-Higgins, M. (1953), Mass transport in water waves, *Philos. Trans. R. Soc. London A*, *245*, 535–581.

Madsen, O. S. (1975), Stability of a sand bed under breaking waves, in *Proceedings of the 14th International Conference on Coastal Engineering*, pp. 776–794, Am. Soc. Civ. Eng., Reston, Va.

Mei, C. C. (1989), *The Applied Dynamics of Ocean Surface Waves*, World Sci., Tokyo.

Mellor, G. (2002), Oscillatory bottom boundary layers, *J. Phys. Oceanogr.*, *32*, 3075–3088.

Middleton, J. F., and J. W. Loder (1989), Skew fluxes in polarized wave fields, *J. Phys. Oceanogr.*, *19*, 68–76.
Nielsen, P. (1992), *Coastal Bottom Boundary Layers and Sediment Transport*, World Sci., Tokyo.
Nielsen, P., and D. P. Callaghan (2003), Shear stress and sediment transport calculations for sheet flow under waves, *Coastal Eng.*, *47*, 347–354.
Phillips, O. (1977), *The Dynamics of the Upper Ocean*, 2 ed., Cambridge Univ. Press, New York.
Pope, S. B. (2000), *Turbulent Flows*, Cambridge Univ. Press, New York.
Priestley, M. (1988), *Non-Linear and Non-Stationary Time Series Analysis*, Academic, San Diego, Calif.
Puleo, J. A., K. T. Holland, N. G. Plant, D. N. Slinn, and D. M. Hanes (2003), Fluid acceleration effects on suspended sediment transport in the swash zone, *J. Geophys. Res.*, *108*(C11), 3350, doi:10.1029/2003JC001943.
Rouse, H. (1937), Modern conceptions of the mechanics of fluid turbulence, *Trans. Am. Soc. Civ. Eng.*, *102*, 463–541.
Ruessink, B., J. Miles, F. Feddersen, R. Guza, and S. Elgar (2001), Modeling the alongshore current on barred beaches, *J. Geophys. Res.*, *106*, 22,451–22,463.
Russell, R., and J. Osorio (1957), An experimental investigation of drift profiles in a closed channel, in *Proceedings of the 6th International Conference on Coastal Engineering*, pp. 171–193, Am. Soc. Civ. Eng., Reston, Va.
Sleath, J. (1984), *Sea Bed Mechanics*, John Wiley, Hoboken, N. J.
Sleath, J. (1999), Conditions for plug formation in oscillatory flow, *Continent. Shelf Res.*, *19*, 1643–1664.
Smith, J. D., and S. McLean (1977), Spatially averaged flow over a wavy surface, *J. Geophys. Res.*, *82*, 1735–1746.
Soulsby, R. (1997), *Dynamics of Marine Sands*, Thomas Telford, London.
Stauble, D. K., and M. A. Cialone (1997), Sediment dynamics and profile interactions: Duck94, in *Proceedings of the 25th International Conference on Coastal Engineering*, pp. 3921–3934, Am. Soc. Civ. Eng., Reston, Va.
Thornton, E., R. Humiston, and W. Birkemeier (1996), Bar/trough generation on a natural beach, *J. Geophys. Res.*, *101*, 12,097–12,110.
Trowbridge, J., and Y. Agrawal (1995), Glimpses of a wave boundary layer, *J. Geophys. Res.*, *100*, 20,729–20,743.
Trowbridge, J., and S. Elgar (2001), Turbulence measurements in the surf zone, *J. Phys. Oceanogr.*, *31*, 2403–2417.
Trowbridge, J., and O. Madsen (1984), Turbulent wave boundary layers: 2. Second-order theory and mass transport, *J. Geophys. Res.*, *89*, 7999–8007.
Trowbridge, J., and D. Young (1989), Sand transport by unbroken water waves under sheet flow conditions, *J. Geophys. Res.*, *94*, 10,971–10,991.
van Hardenberg, B., A. Hay, Y. Sheng, and A. Bowen (1991), Field measurements of the vertical structure of suspended sediment, in *Coastal Dynamics 1991*, pp. 300–312, Am. Soc. Civ. Eng., Reston, Va.
van Rijn, L. (1984), Sediment pick-up functions, *J. Hydraul. Eng.*, *110*, 1494–1502.
van Rijn, L., and F. J. Havinga (1995), Transport of fine sands by currents and waves II, *J. Waterway. Port Coastal Ocean Eng.*, *121*, 123–133.

J. S. Allen and P. A. Newberger, College of Oceanic and Atmospheric Sciences, Oregon State University, Corvallis, OR 97331, USA.
S. M. Henderson, Scripps Institution of Oceanography, Center for Coastal Studies, University of California, San Diego, 9500 Gilman Drive, La Jolla, CA 92093-0209, USA. (shenders@coast.ucsd.edu)